

Anatoliy Khalin¹, Nataliya Kizilova ²

Performance comparison of different aerodynamic shapes for autonomous underwater vehicles

A brief review of the existing autonomous underwater vehicles, their types, design, movement abilities and missions is presented. It is shown, the shape optimization design and enhancement of their efficiency is the main problem for further development of multipurpose glider technologies. A comparative study of aerodynamic performance of three different shape designs (the airfoil NACA0022 based (I), flattened ellipsoidal (II) and cigar-type (III) bodies of the same volumes) has been carried out. Geometrical modelling, meshing and computational fluid dynamics (CFD) simulations have been carried out with AnSys15.0. The pathlines and wall shear stress distributions have been computed to understand the advantages and disadvantages of each shape. The lift and drag coefficients, aerodynamic quality, power index and pitching moment have been computed. The higher efficiency of the shape I/shape II at higher/lower angles of attack ($> 20^\circ$ and $< 20^\circ$) has been found. The shape III develops high speeds at the same angles of attack and has higher manoeuvrability at relatively low aerodynamic quality. The comparative analysis of the flow capabilities of studied autonomous undersea vehicles proposes some design improvement for increasing their energy efficiency and flow stability.

1. Introduction

More than two third of the Earth's surface is covered by oceans, and this area determines global heat and mass transfer with the ocean streams, water evaporation and atmospheric flows. The pressure, temperature and salinity distributions in the world ocean determine climate on the planet, marine biology, wind strength and direction, soil erosion, harvest and all other aspects of human living. In spite of

✉ N. Kizilova, e-mail: n.kizilova@gmail.com

¹V.N. Karazin Kharkov National University, Kharkiv, Ukraine. E-mail: khalinx21@gmail.com

²Warsaw University of Technology, Institute of Aeronautics and Applied Mechanics, Warsaw, Poland.



© 2019. The Author(s). This is an open-access article distributed under the terms of the Creative Commons Attribution-NonCommercial-NoDerivatives License (CC BY-NC-ND 4.0, <https://creativecommons.org/licenses/by-nc-nd/4.0/>), which permits use, distribution, and reproduction in any medium, provided that the Article is properly cited, the use is non-commercial, and no modifications or adaptations are made.

high significance of the knowledge on ocean physics and biology, we little know about life at the bottom of the ocean, formation of the giant surface waves and high-energy internal ocean waves, genesis and early detection of the earthquakes, tornados, recognition of schools of fish and plankton, oil spills, liquid and solid pollutions [1]. During the last decades, a visible breakthrough in this area has been connected to novel glider technologies for autonomous underwater vehicles (AUVs) and new concepts of their design, hydromechanics, tasks, behaviour, interaction, communication, and control [2, 3]. The UAVs have already shown their utility for monitoring the coastal, meso- and submesoscale dynamics, data sampling for ocean modelling, acoustic detection of biological and geological activity, transport of water, food and energy [2]. Based on the swarm work of UAVs, the concept of the Internet of Underwater Things (IoUT) has appeared as a world-wide network of smart interconnected underwater objects that enables permanent monitoring of vast unexplored underwater areas [4].

In the first missions on research and technological exploitations, data collection were carried out by large submarines (Manned Submersive Vehicles, MSV) with fuel, atomic or electric engines. Such missions needed considerable deposits of fuel, oxygen, drinking water, and food for the crew. Modern unmanned AUVs are compact, light, fast and do not need any additional load. They can use the fuel-free gliding flow principles and a small electric engine with a propeller for manoeuvres. The demands for the AUV missions include short and long durations (from 2 weeks to 6 months), low and high depth (from 200 m to > 5 km), low mass in air (from 50 to 100 kg), relatively low speed (typically 20–50 cm/s), and can operate in all possible weather conditions [2, 3]. The swarms of AUVs can share their tasks, and communicate with each other via optical, acoustical or other wireless sensors. The leader can use a surface R/T communication with the convoying ship(s) or stationary land station(s).

The design and technologies needed for efficient civil and military underwater tasks have been elaborated and developed during many decades. Modern technologies of AUVs came from the previously elaborated and implemented approaches of the ROV (Remotely Operated Vehicle), tethered vehicles, and UUVs (Unmanned Untethered Vehicles) [5]. The first truly autonomous type of submarines were torpedoes used for military purposes [6].

2. AUV: main types, design, missions, principles of motion

The gliding flow of AUV is based on small changes in its buoyancy [7]. In the upper point of the glider's trajectory, the seawater is pumped into a tank that makes the glider heavier and it starts sinking (Fig. 1a, b). During this motion due to the streamline shape and wings/fins the pressure differences at the upper and lower surfaces produce the lifting force, and the glider starts to float up (Fig. 1b, c). In a certain instant the water is pumped away that increases the velocity of emersion and the glider reaches its upper location (Fig. 1d). There it can either repeat the

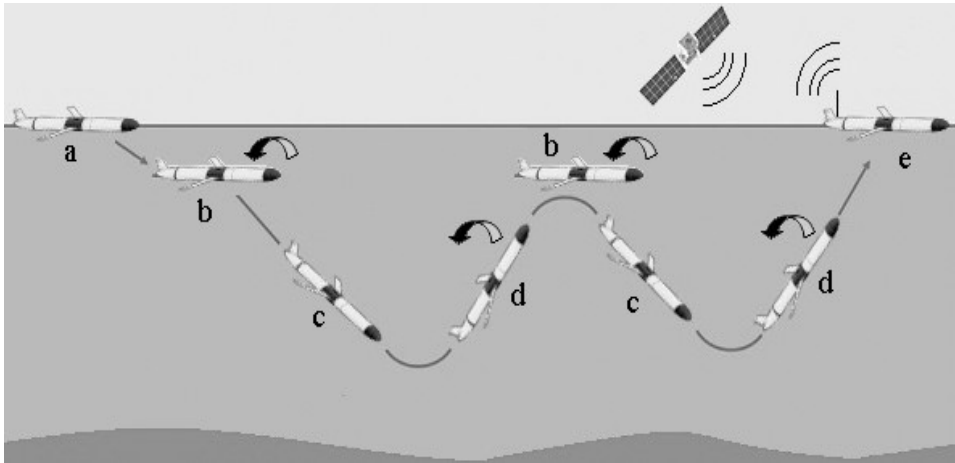


Fig. 1. One cycle of the saw tooth pattern with the phases of float (a), water uptake (b), sink (c), lift (d), upper point and communication (e)

gliding cycle or rise an antenna and communicate with coordinator(s) via wireless R/T, GPS navigation, Iridium satellite and others (Fig. 1e). The motion of gliders is noiseless due to their low speed (~ 0.4 m/s) and absence of engines. They have low power consumption for the water pumping and favourable price-efficiency ratio. In some gliders, the pumping and redistribution of special internal fluids between the tanks is used for the flow stabilization purposes. Additional engine(s) can be used for operating of the robotic arm (manipulator) for the soil/water sampling, mounting/collection of sensors, and other activity. The main modes of the movement of gliders are the saw tooth (Fig. 2a) and spiral (Fig. 2b) up/down patterns [8]. Therefore, the flow parameters, lift and drag forces acting on the AUV

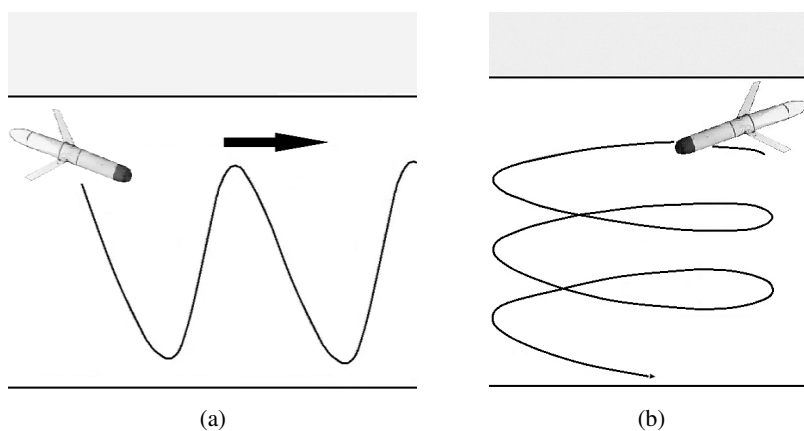


Fig. 2. Two types of gliding trajectories: sawtooth (a) and spiral (b) patterns

at different positive and negative angles of attack are of great interest for the efficiency estimation and flow stability of the gliders. Note, the gliding is operated at a constant angle of attack for the both types of trajectories. An approximate schema of the internal construction of the glider is given in Fig. 3.

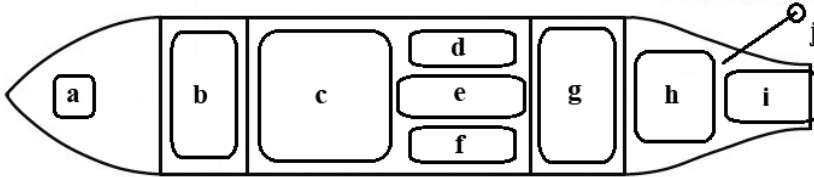


Fig. 3. Internal construction of a typical glider: a – sensors (altimeter, etc.), b – buoyancy pump, c – payload section, d – computer and modem, e – battery pack, f – robotic arm unit, g – additional pump(s) for yaw movement, h – inflatable bladder, i – propeller/steering fin unit, j – antennae

The design of the engine called Hydroglider based on the changes in buoyancy due to the water pumping in and out and a sawtooth motion was submitted by Evan Fellon as a patent in the early 1960s. It was not an unmanned vehicle, and a man for the water pumping and flow control was foreseen in this patent. In 1989, famous oceanographer Henry Stommel introduced his concept of an unmanned underwater glider based on the temperature difference between the surface waters (atmospheric temperature) and deep ocean waters ($\sim 2\text{--}4^\circ\text{C}$) [9]. The concept was called Slocum, after the first man who solely sailed around the world at the end of the XIX century. Several years later after Stommel's article, the first prototypes (Fig. 4) Slocum (Webb Research Corporation), Spray (Scripps Institution of Oceanography) and Seaglider (School of Oceanography, University of Washington) were elaborated [10–13].

In 1989 the “Slocum Mission” for oceanographic studies has been started and in 1991 the first Slocum prototype and thermal engine were tested. The first Autonomous Oceanographic Sampling Networks paper appeared in the *Oceanography Journal* in 1993 [14]. A shallow-water glider ALBAC was developed in the lab of Tamaki Ura (University of Tokyo) in 1992 [15]. It was not supplied by a pumping engine and used a weight dropped out at a certain depth to drive the AUV in each single dive cycle. It also used a moving internal mass to control the flow stability against possible pitch and roll. In 2003, the Canadian Navy conducted the tests of SPAWAR on three Slocum electric gliders in the Gulf of Mexico. At the end of 2003, an oceanographic glider project Autonomous Ocean Sampling Network (AOSN II) was prepared for the research missions for > 6 weeks conducted in Monterey Bay CA. In September – November of 2004, the Spray glider travelled ~ 600 miles during ~ 1 month across the Gulf Stream, at the speed ~ 0.5 miles per hour or 12 miles per day. In 2004, SeaGliders operated through a typhoon off East Asia. In 2005, two Sea Gliders travelled from Washington coast to Hawaii with a 6 month mission. In 2005, a lunch of gliders from US submarine was tested.

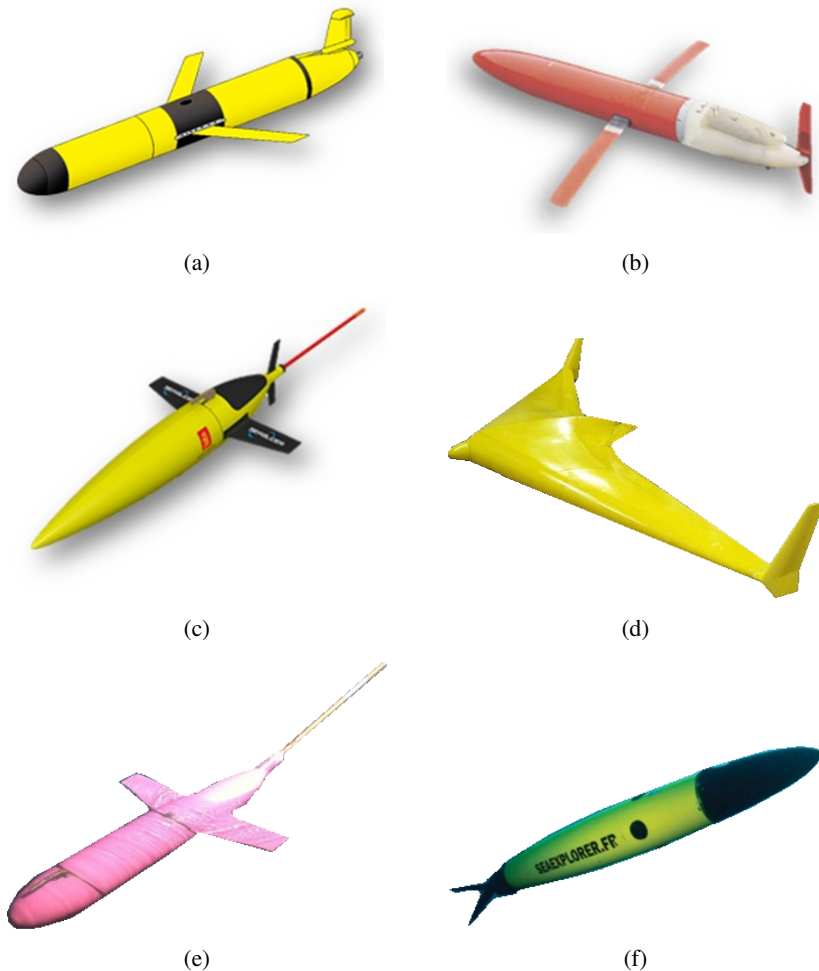


Fig. 4. Legacy gliders Slocum (a); Spray (b); and Seaglider (c); XRay (d); Deepglider (e) and Seaexplorer (f) (from [15, 23, 24])

The very first gliders Slocum electric, Spray and Seaglider had been called ‘legacy gliders’, while XRay Liberdade (US Navy Office of Naval Research), Deepglider (University of Washington School of Oceanography), SeaExplorer (ACSA company), and others have appeared later [2, 3, 5, 16]. The Chinese glider Haiyan7000 is slower in comparison with other AUVs but it is more energy efficient and enables longer surveillance capacity [17]. The electrical engine/battery [18], the thermal engines based on the temperature gradient [13], hybrid propulsion systems [19] or used ocean waves [20], solar energy [21], and fuel cells [22] have been elaborated and tested for the gliders’ missions, as well as hybrid-driven models [23]. The groups working in AUV area include large universities, research institutions and business like University of Washington, Massachusetts Institute of Technology,

Florida Atlantic University, Johns Hopkins University, Autonomous Systems Laboratory, University of Hawaii, Virginia Polytechnic Institute, Autonomous Undersea Systems Institute, Woods Hole Oceanographic Institution (WHOI), Monterey Bay Aquarium Research Institute (MBARI), Naval Postgraduate School and others [5, 16]. The search for other alternative energy sources to optimize the time of missions and energy consumption is an urgent task nowadays.

Different gliders possess quite different operating parameters (Table 1) depending on their missions. For example, XRay Liberdade developed for military purposes, has payload of about 850 kg, while Slocum thermal can carry max 2 kg only but performs an autonomous mission up to 5 years. As one can see, the fastest designs are XRay Liberdade and SeaDiver, they also have a largest payload. The greatest range and least energy consumptions has the Slocum thermal concept, while the Deepglider can reach the deepest distances, that is it was elaborated for.

Despite significant progress in the AUV technology, there are problems of the shape and trajectory optimization, flow regime and motion control [24, 25], and decision-making in a team of AUVs [26] to be solved. Thorough FEM computations and performance analyses play an essential role in the detailed design [23, 27], testing [28] and optimization of the shape [27, 29], trajectory [30], flow regime,

Table 1.

Operating characteristics of some types of gliders

Name	Depth (m)	Range (km)	Payload (kg)	Weight (kg)	Horiz. speed (cm/s)	Glide angle (°)	Energy supply	Dimensions ($L \times D$, cm)
Slocum electric	4–200	1500–2300, 30 days	3–4	52	30–40	35	260 Alkaline C cells, 8MJ	150×21.3
Spray	to 1500	3500–7000, 330 days	3.5–51.8	51.8	35–45	9–25	52 Li CSC DD cells, 13MJ	200×20
Seaglider	1000	4600–6000, 220 days	25	52	40–45	8–70	81 Li D cells, 10MJ	180×30
Slocum thermal	4–1200	40,000	2	60	40	19–25	Thermal engine, Alkaline batteries	150×21.3
Deepglider	6000	8500	25	62	25	14–45	Li CSC cells	180×30
X-Ray Liberdade	365	1500	850	–	50–180	–	–	–
SeaExplorer	700	1 200	8	59	50	–	Rechargeable Li-ion	270
Wing-type (Fig. 5a)	20–100	1600	540	60	50–100	15–20	Six packs of Li batteries 12 V 40 AH	800×400×200
Ellipsoid (Fig. 5b)	–	–	–	70	–	15–30	–	900×400×200
Cigar-type (Fig. 5c)	17	2000	12	30	35	15–40	12V batteries	900×50

stability and control [23, 31–33] for different AUV missions. In this paper, the performance of the wing-type based on the popular NACA0022 air foil (Fig. 5a), ellipsoidal (Fig. 5b) and cigar-type (Fig. 5c) shapes is studied. Their operating characteristics [34] are presented in Table 1. The first glider is designed for high speed delivery of heavy cargo, while the third one (Fig. 5c) without wings but with a low drag had been designed for a shallow water missions with small payload and moderate speeds [35].

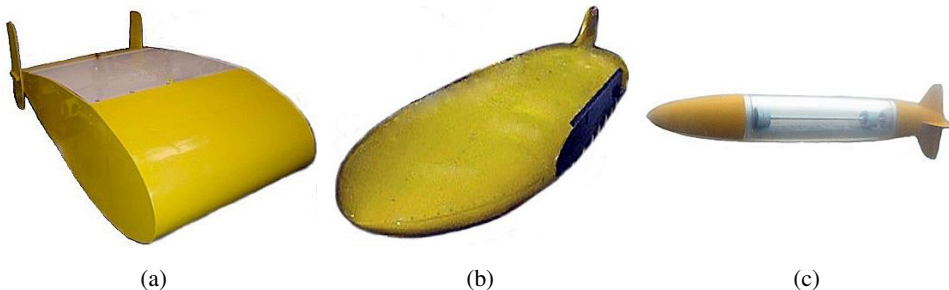


Fig. 5. The prototypes of the SeaDiver (a), ellipsoidal (b) and GreyWhale (c) gliders (from [34, 35])

3. CFD analysis of a steady sawtooth motion at a constant angle of attack

Actually, detailed data on shape and performance characteristics of the AUVs is hardly available because of high competition at the market. Therefore, the most available and simple shapes elaborated and tested at Laboratoire des Systèmes Navals Complexes (Toulon, France) have been used for the present study. The shape I of the SeaDiver (Fig. 5a) followed the NACA0022 air foil with dimensions given in Table 1 [34]. Aerodynamic properties of the NACA0022 air foil have been studied in numerous experiments and CFD computations, and the corresponding data are presented for different Reynolds number, ambient temperatures and angles of attack [36, 37]. Despite the air foil and its computational models, the Seadiver has much shorter width and, thus, the bigger influence of the lateral surfaces in comparison to the wings with the same hydrodynamic profile. The ballast chamber is positioned in the frontal part of SeaDiver and is optimized for efficient conversion of the up-and-down movement into horizontal displacement due to the lift force. SeaDiver fulfil sinusoidal-like saw tooth movements from the sea surface down to 300 feet underwater [34].

The shape II (Fig. 5b) is a flattened ellipsoidal shape with given dimensions (Table 1). Due to the smooth lateral surfaces, it is more stable and manoeuvrable than the SeaDiver. An additional stabilization is provided by short side fins like the ones in the SeaDiver (Fig. 5a, 5b). The shape III for the GreyWhale glider is cigar-type with a pointed frontal and cylindrical rear parts (Fig. 5c). It moves with the amplitude of the ~ 13 – 14 m with the range 82.5 m, speed 36 cm/s and

the angle of attack $\alpha = 11^\circ$ averaged over a diving cycle [35]. Only the averaged data presented in Table 1 are available for validation of the models studied. In the test studies, the shape I was found very efficient in the meaning of the lift/drag ratios but demonstrated instability during the manoeuvres that could be connected to the flow disturbances by the acute ages at the sides of the shape. The shape II had similar lift/drag ratios but better manoeuvrability, probably, due to its smoother design. The shape III is very popular nowadays but the problem of its shape optimization is not solved yet, as one can see from the variety of shape modifications presented in Fig. 4a–4c, 4e, 4f.

For the comparative numerical study of the hydraulic properties and efficiency, the shapes have been scaled to the same volume with the dimensions related to the original proportions. The average volume was taken as $V_0 = 0.3528 \text{ m}^3$, and the corresponding dimensions $L \times H \times W$ (length \times height \times width) were chosen as

I. SeaDiver: $L \times H \times W = 1.7 \times 0.8 \times 0.7 \text{ m}$,

II. Flattened ellipsoidal: $L \times H \times W = 1.7 \times 0.72 \times 0.26 \text{ m}$,

III. GeayWhale: $L \times H \times W = 2.3 \times 0.43 \times 0.43 \text{ m}$.

The chosen dimensions have been slightly changed in comparison to the corresponding data given in Table 1 to provide the same volume of the AUVs. All the shapes I–III are symmetric relative to the vertical plane and the $W/2$ of the shape has been modelled.

Steady fluid flow over the glider surface fixed at a given angle of attack α produces the lifting force F_L (positive upwards) and the drag force F_D which are vertical and horizontal components of the force acting onto the glider and balanced by the gravitation, buoyant and resistive forces

$$F_L = \frac{1}{2} \rho u^2 C_L A, \quad F_D = \frac{1}{2} \rho u^2 C_D S, \quad (1)$$

where C_L and C_D are non-dimensional lift and drag coefficients, u is the flow velocity, A and S are lifting and frontal surfaces of the body at the given angle of attack.

The total force $\vec{F} = F_L \vec{n} + F_D \vec{\tau}$ results from the dynamical pressure

$$P = \frac{\rho}{2} (u_h^2 + u_v^2)$$

differences acting on the upper and lower part of the surface, where u_h and u_v are horizontal and vertical components of the fluid flow governed by the corresponding fluid dynamic equations for the turbulent subsonic model.

The comparative analyses of the aerodynamic performance are carried out based on the dependencies of the C_L and C_D coefficients on the angle of attack, $C_L(C_D)$, $C_D/C_L(\alpha)$ (aerodynamic quality), $C_L^3/C_D^2(C_L)$ (power index), and $C_M(\alpha)$. Here

$$C_M = \frac{M}{PAI}, \quad (2)$$

where M is the pitching moment trying to rotate the body around its centre of mass, l is the length of the chord of the airfoil. The power index $Pi = C_L^3/C_D^2$ determines the power required for maintaining a fixed position of the body in the flow $N = f(Pi)\sqrt{2f/\rho S}$ [38]. The best climb and max endurance flight will be achieved at the max Pi values [39].

Geometric modelling, meshing and CFD computations have been carried out on AnSys 15.0 software. The size of used domain for the flow modelling was $25 \times 20 \times 10$ m (Fig. 6) that corresponds to the AnSys Fluent recommendations for the 3D airfoil computations with $h/L \leq 0.05$, $H/L \geq 0.4$, $W/L \geq 0.2$, $L_1/L_2 \sim 0.4$ [40], where H , W , L are the height, weight and length of the computational domain, L_1 is the length from the inlet to the centre of mass of the studied body, and $L_2 = L - L_1$, h is the longitudinal length of the shape.

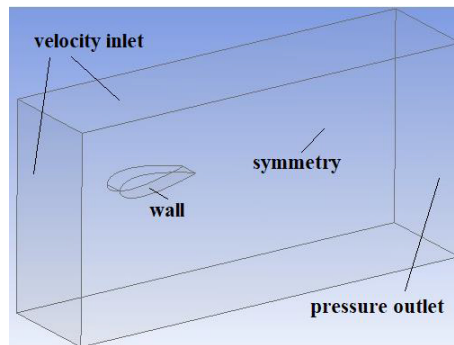


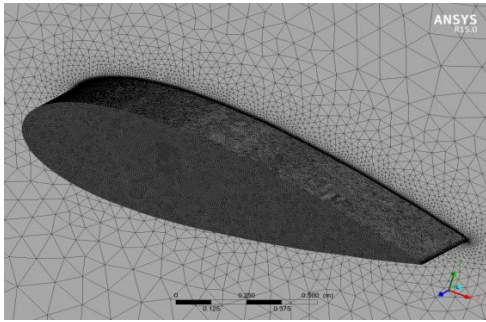
Fig. 6. The example of computational domain with boundary conditions used for the CFD modelling

Tetrahedral meshes with prismatic layers to model the flow in boundary layer (BL) areas have been with ANSYS ICEM software. Such types of models have the capability of capturing not only turbulent flow in domain, but also laminar regions which potentially could have great influence on aerodynamic performance [41]. The mesh generated for the shapes I, II, III are presented in Fig. 7. The optimal number N of cells has been chosen by the test computations on the grids with increasing number of the cells at direct monitoring of the residuals ($= 10^{-3}$), and was set as $N = 4022886$ (shape I), $N = 4261944$ (shape II), $N = 4006166$ (shape III). The boundary layer at the surface was computed by introduction of $n = 16$ boundary layers with the same growth rate $gr = 1.2$ for all the shapes. The number of the layers has been computed from the BL thickness and skin friction coefficient computed by the Schlichting approximation formula [42].

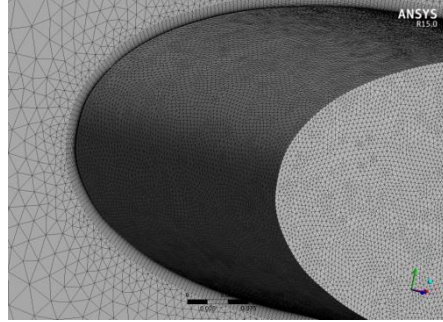
The orthogonal quality of the meshes was quite good, namely

- Shape I: $MOQ = 6.08937e-01$, $MAR = 4.10804e+00$,
- Shape II: $MOQ = 6.35060e-01$, $MAR = 4.54143e+00$,
- Shape III: $MOQ = 6.84554e-01$, $MAR = 4.26646e+00$,

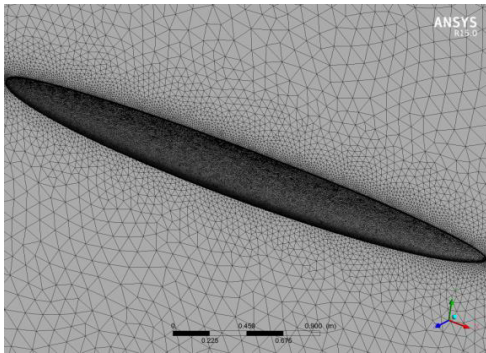
where MOQ = minimum orthogonal quality, MAR = maximum aspect ratio.



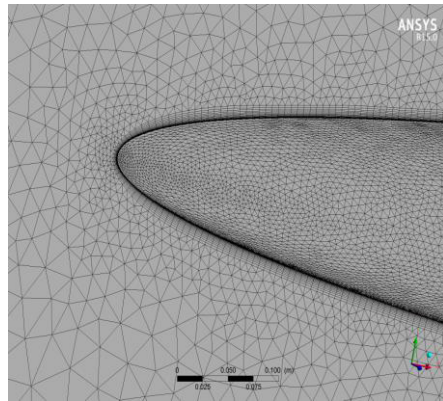
(a)



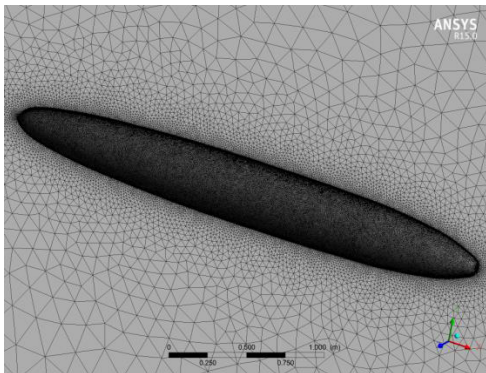
(b)



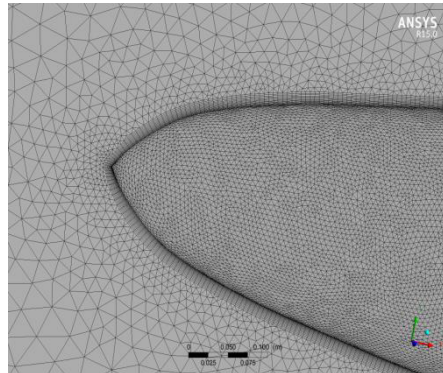
(c)



(d)



(e)



(f)

Fig. 7. The examples of mesh generated for the model I (a, b), II (c, d), III (e, f), their full shapes (a, c, e) and frontal (b, d, f) regions

The following boundary conditions have been used for all the shapes:

- velocity inlet: for inlet surfaces of the computational domain (Fig. 6);
- pressure outlet: for outlet surfaces of the computational domain (Fig. 6);
- symmetry: for the vertical symmetry planes of the shapes;
- wall: for all gliders' surfaces.

The Reynolds number $Re = \rho v D_h \mu$, where D_h is the characteristic length of the cross-sectional area of the shape computed for the salt water flow with real dimensions of the shapes and their average velocities (Table 1), is within the range $Re = (2.7-8.2) \cdot 10^5$. Therefore, the standard k- ϵ turbulent model with near-wall treatment by standard wall functions has been used. The turbulent parameters at the velocity inlet and pressure outlet have been taken as follows:

- turbulence intensity = 0.1 % (typical for external flows [40]);
- turbulent viscosity ratio = 1 (typical for external flows [40]);
- intermittency = 1 (corresponds to fully developed turbulent flow).

The material parameters for the sea water have been taken as [34]

- density of salt water: $\rho = 1190 \text{ kg/m}^3$;
- kinematics viscosity at the mean ocean temperature 12.5°C :
 $\nu = 1.225 \cdot 10^{-6} \text{ m}^2/\text{s}$;
- speed of sound: $c = 1500.3 \text{ m/s}$.

The second-order upwind numerical schemes for the turbulent kinetic energy, turbulent dissipation rate and momentum with SMPLE pressure-velocity coupling algorithm have been used. The same model and similar settings have been used in previous computations on the shape I [34].

As the velocity inlet boundary conditions, the constant speeds $u = 52 \text{ cm/s}$ (shape I), $u = 35 \text{ cm/s}$ (models II, III) have been assigned [34, 35]. The angle of attack $\alpha \in [-40^\circ, 40^\circ]$ has been changed with the step of 10° . The pressure and flow distributions around the shapes have been computed, and the C_L and C_D coefficients have been calculated. For the model validation, the 2D computations on the NACA0022 airfoil [38] have been carried out with the same computational domain, mesh and FLUENT settings. The computation results of the $C_L(\alpha)$ and $C_D(\alpha)$ dependencies have been compared to the experimental data for the same aerodynamic profile and different Re numbers [36, 37]. The numerical results are presented in the next section.

4. Numerical results and discussion

The computed pressure and velocity distributions around the shapes I–III at the same angles of attack demonstrate similar distributions of the same order of magnitude. The wall shear stress (WSS) distributions are strongly influenced by the shape of the AUV (Fig. 8). The highest values along the fore-part of the shape I increases at higher angles of attack (Fig. 8a, 8b) according to the fluid dynamic theory. Similar regularities are demonstrated by the shape II (Fig. 8c, 8d) and shape III (Fig. 8e, 8f) that confirms physical relevance of the model. The area

of the higher WSS becomes wider for the shape I (Fig. 8b). For the shape II it remains of almost the same size but with twice higher peak values (Fig. 8d). In the case of the shape III, the changes are more crucial and comprise almost all the body (Fig. 8f).

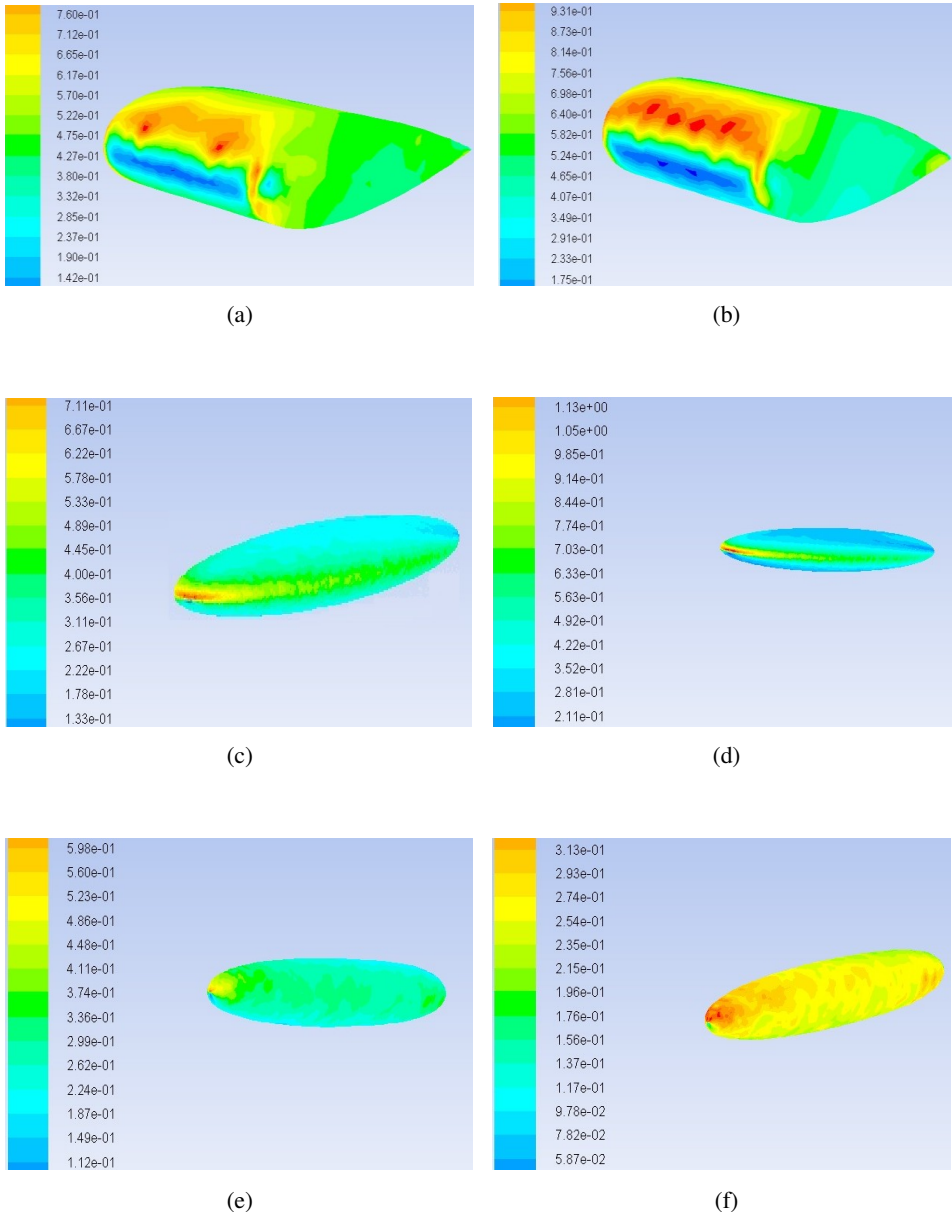


Fig. 8. Computed WSS distributions over the shape for the wind-type (a, b), ellipsoidal (c, d) and cigar-type (e, f) gliders at the angles of attack $\alpha = 10^\circ$ (a, c, e) and $\alpha = 20^\circ$ (b, d, f)

Due to low velocity of motion and the streamline shapes, the wake behind the bodies appears at higher angles of attack $\alpha > 10^\circ$. The side surfaces of the shape I disturb the flow and produce a pair of wakes (Fig. 9). The laminar to turbulent transition at the rear part of the shape I becomes visible at $\alpha \geq 18^\circ$ (Fig. 9b). The shape II produces a similar pair of wakes at $\alpha \geq 10^\circ$. The flow separation appears earlier (at $\alpha \geq 7^\circ$) than for the shape I for the latter has more streamline rear part of its body. At $\alpha = 25^\circ$, the flow separation is located at $\sim 1/3$ of the body length that contributes significantly to the drag coefficient. The shape III produces higher velocities around its body and, therefore, higher WSS, flow separation and single wake at $\alpha \geq 6^\circ$.

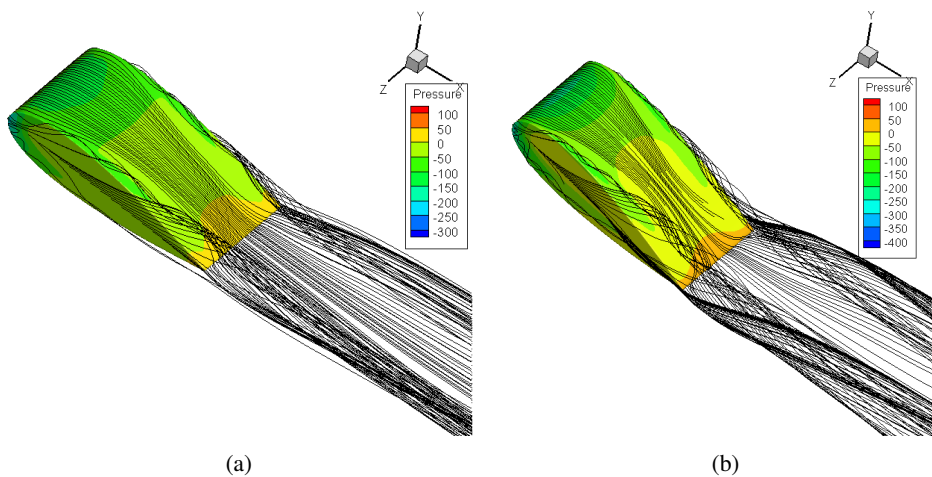
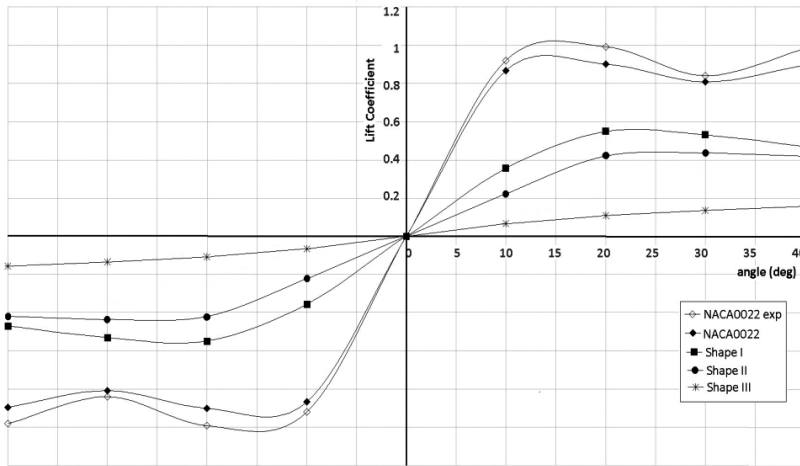


Fig. 9. The computed pathlines outgoing from the sidelines of the horizontal section of the shape I at the angles of attack $\alpha = 10^\circ$ (a) and $\alpha = 20^\circ$ (b)

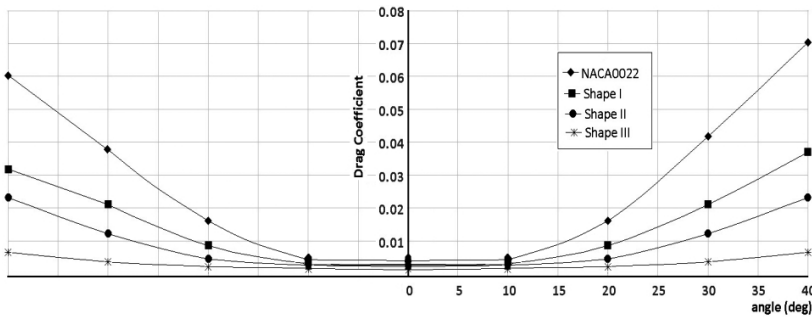
The non-dimensional lift and drag coefficients calculated on (1) by using the flow parameters computed over the corresponding shape are presented in Fig. 10a, 10b. The efficiency of the shapes I and II in the meaning of the lift coefficients are similar, but the shape I has slightly higher lift coefficient with a maximum at $\alpha \sim 20^\circ$. The computed curve $C_L(\alpha)$ exactly corresponds to the similar dependence with a maximum at $\alpha = 19\text{--}25^\circ$ computed for the wind-type shape in [34].

The negative factors of the shapes I, II at higher angles of attack are higher WSS at the frontal part of the body (Fig. 8a, 8b), flow separation and vortex formation at the side walls and at the rear part of the body (Fig. 9). The 2D NACA0022 airfoil has higher C_L values at all the studied angles of attack due to absence of the additional energy loss for skin friction, flow disturbance and viscous dissipation. The computed $C_L(\alpha)$ curve for the 2D shape is in a good correspondence to the experimental data [37].

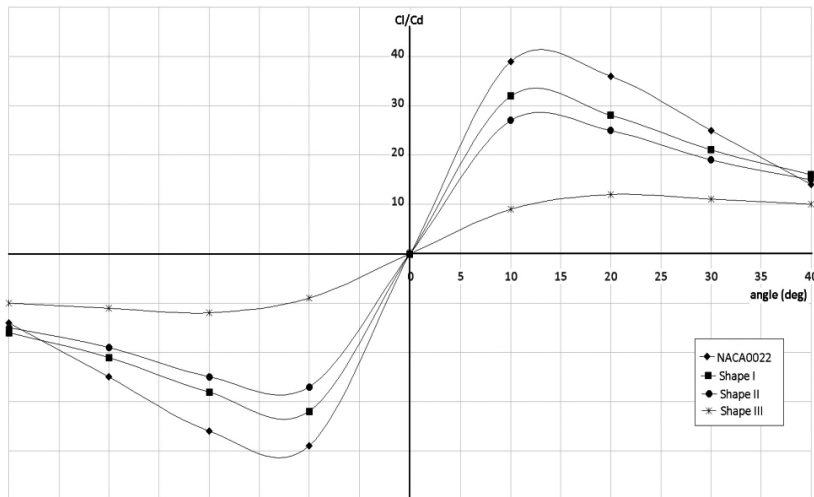
The dependences of the drag coefficients on the angle of attack are presented in Fig. 10b. At $\alpha < 20^\circ$, the drag is negligible lower for the shape II, while at



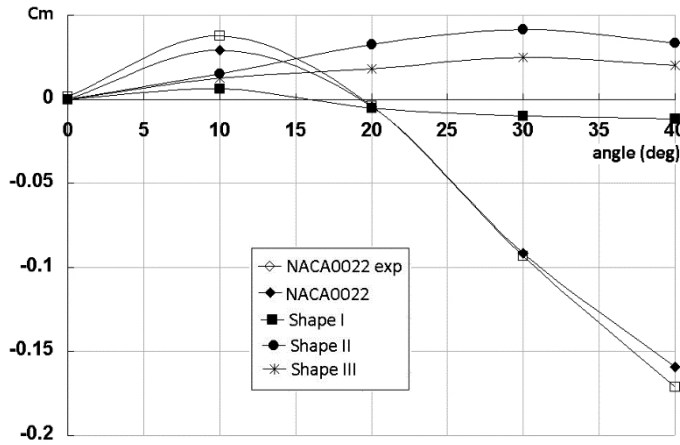
(a)



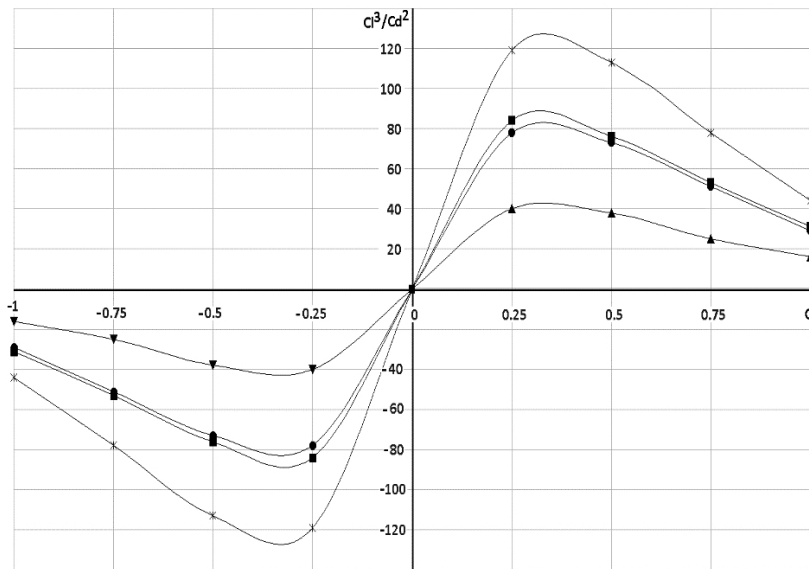
(b)



(c)



(d)



(e)

Fig. 10. The computed dependencies of the lift C_L (a) and drag C_D (b) coefficients, C_L/C_D (c) and C_m (d) indexes on the angle of attack $\alpha \in [0; 40^\circ]$, and the power index $C_L^3/C_D^2(C_L)$ (e)

$\alpha > 20^\circ$ its drag coefficients grows quite fast and becomes essentially higher than those for the shape I. The shape III possesses much lower drag coefficient at lower lift coefficients because of the non-streamline contour of its body. The aerodynamic quality characterized by the C_L/C_D coefficient is higher for the shapes I, II. Both shapes have the same optimal angle of attack $\alpha = 11-16^\circ$ (Fig. 10c). The shape III has lower quality and optimal angles $\alpha = 20-24^\circ$ which are proper to the deep

water gliders (Table 1). The computed angles are close to the corresponding ones established for the same shapes by CFD studies and experimental performance testing [34, 35]. More detailed experimental measurements of the pressures, flows and WSS distributions for the model validation are unavailable.

The pitching moment coefficient C_m confirms experimental observations on low stability and manoeuvrability of the shape I. The curve in Fig. 10d can be inverted through the centre of coordinates. For the shallow water motion, the shape I is stable at $|\alpha| < 20^\circ$ only that may be not enough to produce sufficient lifting force [34]. At higher angles of attack, the motion could be destabilized because internal flows and sea streams may produce a medium amplitude disturbance and the returning force could be either too small or act in the same direction as the disturbance does. Surprisingly, the shape III is quite stable even at higher angles of attack. Perhaps, due to its rocket-type shape, the disturbances can initiate its rotation, which is not crucial due to the axial symmetry. The most stable is the shape II that corresponds to the sea testing of this AUV [34].

The power index dependence confirms the previous conclusions on existing the narrow limits for the optimal angle of attack where the aerodynamic quality coefficient reaches its maximal values for each of the geometric shapes. The values for the shape III are rescaled to be visible in the plots with the coefficients for NACA0022 airfoil (Fig. 10e), but its C_L^3/C_D^2 (C_L) dependence has the same characteristic features like initial growth with C_L followed by the maximum peak and later decrease with C_L as for the shapes I and II. Such a type of dependency is also proper to the airfoils [38–40], but the computed values for the gliders are lower than the known ones for the elongated wings because of the high influence of the side effects of the glider geometries (e.g., much smaller widths in comparison to the wings of the aircrafts).

Therefore, three studied shapes have different advantages/disadvantages at the low/high angles of attack introduced by the side walls and high WSS at the front surface (shape I), side wakes (shape II) and non-streamline contour (shape III). The combination of the streamline shape I with smoothed sides like in the shape II can be considered as an improvement of the shape I. The shape II produces smaller side wakes especially at small angles of attack $|\alpha| < 20^\circ$ during the shallow water missions. The deep water strategies need the more elongated design like the flattened shape III, i.e., a combination of the shapes II and III. The presented computational results must be repeated for the newly proposed cross sections and additional fins stabilizing the flow at the rear and medium cross-sections (Table 1) that will be done in the next studies.

5. Conclusions

In this paper, the comparative study of the aerodynamic characteristics during the sawtooth sliding of three AUV prototypes designed and tested by Laboratoire des Systèmes Navals Complexes (Toulon, France) have been studied using CFD

simulations. After the detailed analysis of the existing shapes, three different types of them have been chosen: the streamline wing-type shape, the flattened ellipsoid, and the cylindrical elongated cigar-type shape. The dimensions of the shapes have been chosen according to existent prototypes and the condition of the same total volume that means the equivalence of the payload volumes for the shapes chosen. Geometric modeling, meshing and CFD computations have been carried out in An-Sys15.0 software. The numerical procedure has been validated on the NACA0022 airfoil that had been computed and analysed at different flow regimes, and the detailed results can be found in the textbooks and reference books [38, 39, 43].

It was shown; the pathlines and wall shear stress distributions have been computed to understand the advantages and disadvantages of each shape. The lift and drag coefficients, aerodynamic quality, power index and pitching moment have been computed. The higher efficiency of the shape I/shape II at higher/lower angles of attack ($> 20^\circ$ and $< 20^\circ$) has been found. The shape III develops higher speeds at the same angles of attack and has higher manoeuvrability at relatively low aerodynamic quality. Flow capabilities and shape optimization design for autonomous undersea vehicles have been discussed.

Manuscript received by Editorial Board, December 04, 2018;
final version, April 01, 2019.

References

- [1] F. Muttin. Umbilical deployment modeling for tethered UAV detecting oil pollution from a ship. *Applied Ocean Research*, 33(4):332–343, 2011. doi: [10.1016/j.apor.2011.06.004](https://doi.org/10.1016/j.apor.2011.06.004).
- [2] D. Meyer. Glider Technology for ocean observations: a review. *Ocean Science Discussions*, 1–26, 2016. doi: [10.5194/os-2016-40](https://doi.org/10.5194/os-2016-40).
- [3] S. Ruiz, B. Garau, M. Martinez-Ledesma, B. Casas, A. Pascual, G. Vizoni, J. Bouffard, E. Heslop, A. Alvarez, P. Testor, and J. Tintoré. New technologies for marine research: five years of glider activities at IMEDEA. *Scientia Marina*, 76:261–270, 2012. doi: [10.3989/scimar.03622.19L](https://doi.org/10.3989/scimar.03622.19L).
- [4] M.C. Domingo. An overview of the internet of underwater things. *Journal of Network and Computer Applications*, 35:1879–1890, 2012. doi: [10.1016/j.jnca.2012.07.012](https://doi.org/10.1016/j.jnca.2012.07.012).
- [5] J. Yuh, G. Marani, and D.R. Blidberg. Applications of marine robotic vehicles. *Intelligent Service Robotics*, 4:221–231, 2011. doi: [10.1007/s11370-011-0096-5](https://doi.org/10.1007/s11370-011-0096-5).
- [6] E. Gray. *The Devil's Device: Robert Whitehead and the history of the Torpedo*. Naval Institute Press, Annapolis, 1991.
- [7] N.D. Kraus. *Wave glider dynamic modeling, parameter identification and simulation*. PhD Thesis, University of Hawaii, 2012.
- [8] J.G. Graver. *Underwater gliders: dynamics, control and design*. PhD Thesis, Princeton University, NJ 08544, 2005.
- [9] H. Stommel. The Slocum Mission. *Oceanography*, 2(1):22–25, 1989. doi: [10.5670/oceanog.1989.26](https://doi.org/10.5670/oceanog.1989.26).
- [10] J. Sherman, R.E. Davis, W.B. Owens, and J. Valdes. The autonomous underwater glider “Spray”. *IEEE Journal of Oceanic Engineering*, 26(4):437–446, 2001. doi: [10.1109/48.972076](https://doi.org/10.1109/48.972076).

- [11] C.C. Eriksen, T.J. Osse, R.D. Light, T. Wen, T.W. Lehmann, P.L. Sabin, J.W. Ballard, and A.M. Chiodi. Seaglider: a long range autonomous underwater vehicle for oceanographic research. *IEEE Journal on Oceanic Engineering*, 26(4):424–436, 2001. doi: [10.1109/48.972073](https://doi.org/10.1109/48.972073).
- [12] M.Y. Javaid, M. Ovinis, T. Nagarajan, and F.B.M. Hashim. Underwater gliders: a review. *MATEC Web of Conferences*, 13:02020–5, 2014. doi: [10.1051/mateconf/20141302020](https://doi.org/10.1051/mateconf/20141302020).
- [13] D.C. Webb, P.J. Simonetti, and C.P. Jones. SLOCUM, an underwater glider propelled by environmental energy. *IEEE Journal of Oceanic Engineering*, 26(4):447–452, 2001. doi: [10.1109/48.972077](https://doi.org/10.1109/48.972077).
- [14] T.B. Curtin, J.G. Bellingham, J. Catipovic, and D. Webb. Autonomous oceanographic sampling networks. *Oceanography*, 6(3):86–94, 1993. doi: [10.5670/oceanog.1993.03](https://doi.org/10.5670/oceanog.1993.03).
- [15] K. Kawaguchi, T. Ura, M. Oride, and T. Sakamaki. Development of shuttle type AUV ALBAC and sea trials for oceanographic measurement. *Journal of the Society of Naval Architects of Japan*, 178:657–665, 1995 (in Japanese). doi: [10.2534/jjasnaoe1968.1995.178_657](https://doi.org/10.2534/jjasnaoe1968.1995.178_657).
- [16] S. Wood. Autonomous underwater gliders. In A.V. Inzartsev, Editor, *Underwater Vehicles*, chapter 26, pages 505–530, IntechOpen, 2009. doi: [10.5772/6718](https://doi.org/10.5772/6718).
- [17] D. Tsering. China deep-sea exploration: intention and concerns. *Maritime Affairs: Journal of the National Maritime Foundation of India*, 13(1):91–98, 2017. doi: [10.1080/09733159.2017.1326570](https://doi.org/10.1080/09733159.2017.1326570).
- [18] Ø. Hasvold, N.J. Størkersen, S. Forseth, and T. Lian. Power sources for autonomous underwater vehicles. *Journal of Power Sources*, 162(2):935–942, 2006. doi: [10.1016/j.jpowsour.2005.07.021](https://doi.org/10.1016/j.jpowsour.2005.07.021).
- [19] X. Wang, J. Shang, Z. Luo, L. Tang, X. Zhang, and J. Li. Reviews of power systems and environmental energy conversion for unmanned underwater vehicles. *Renewable and Sustainable Energy Reviews*, 16(4):1958–1970, 2012. doi: [10.1016/j.rser.2011.12.016](https://doi.org/10.1016/j.rser.2011.12.016).
- [20] S. Willcox, J. Manley, and S. Wiggins. The wave glider, an energy-harvesting autonomous surface vessel. *Sea Technology*, 50(11):29–32, 2009.
- [21] T.B. Curtin, D.M. Crimmins, J. Curcio, M. Benjamin, and C. Roper. Autonomous underwater vehicles: trends and transformations. *Marine Technology Society Journal*, 39(3):65–75, 2005. doi: [10.4031/002533205787442521](https://doi.org/10.4031/002533205787442521).
- [22] S. Wang, C. Xie, Y. Wang, L. Zhang, W. Jie, and S.J. Hu. Harvesting of PEM fuel cell heat energy for a thermal engine in an underwater glider. *Journal of Power Sources*, 169(2):338–346, 2007. doi: [10.1016/j.jpowsour.2007.03.043](https://doi.org/10.1016/j.jpowsour.2007.03.043).
- [23] K. Isa, M.R. Arshad, and S. Ishak. A hybrid-riven underwater glider model, hydrodynamics estimation, and analysis of the motion control. *Ocean Engineering*, 81:111–129, 2014. doi: [10.1016/j.oceaneng.2014.02.002](https://doi.org/10.1016/j.oceaneng.2014.02.002).
- [24] M.S. Stewart and J. Pavlos. A means to networked persistent undersea surveillance. In *Submarine Technology Symposium STS*, pages 2–38, 2006.
- [25] APL. The Applied Physics Laboratory Biennial 2007 Report, College of Ocean and Fishery Sciences, University of Washington, 2007.
- [26] T. Praczyk and P. Szymak. Decision system for a team of autonomous underwater vehicles – Preliminary report. *Neurocomputing*, 74(17):3323–3334, 2011. doi: [10.1016/j.neucom.2011.05.013](https://doi.org/10.1016/j.neucom.2011.05.013).
- [27] M.Y. Javaid, M. Ovinis, F.B.M. Hashim, A. Maimun, Y.M. Ahmed, and B. Ullah. Effect of wing form on the hydrodynamic characteristics and dynamic stability of an underwater glider. *International Journal of Naval Architecture and Ocean Engineering*, 9(4):382–389, 2017. doi: [10.1016/j.ijnaoe.2016.09.010](https://doi.org/10.1016/j.ijnaoe.2016.09.010).
- [28] Y. Singh, S.K. Bhattacharyya, and V.G. Idichandy. CFD approach to modelling, hydrodynamic analysis and motion characteristics of a laboratory underwater glider with experimental results. *Journal of Ocean Engineering and Science*, 2(2):90–119, 2017. doi: [10.1016/j.joes.2017.03.003](https://doi.org/10.1016/j.joes.2017.03.003).

- [29] C. Sun, B. Song, P. Wang, and X. Wang. Shape optimization of blended-wing-body underwater glider by using gliding range as the optimization target. *International Journal of Naval Architecture and Ocean Engineering*, 9(6):693–704, 2017. doi: [10.1016/j.ijnaoe.2016.12.003](https://doi.org/10.1016/j.ijnaoe.2016.12.003).
- [30] S. Zhang, J. Yu, A. Zhang, and F. Zhang. Spiraling motion of underwater gliders: Modeling, analysis, and experimental results. *Ocean Engineering*, 60:1–13, 2013. doi: [10.1016/j.oceaneng.2012.12.023](https://doi.org/10.1016/j.oceaneng.2012.12.023).
- [31] D.C. Seo and C.D. Williams. CFD Predictions of drag force for a Slocum ocean glider. Technical Report no. TR-2010-07. NRC Canada, 2010. doi: [10.4224/17210700](https://doi.org/10.4224/17210700).
- [32] K. Alam, T. Ray, and S.G. Anavatti. Design and construction of an autonomous underwater vehicle. *Neurocomputing*, 142:16–29, 2014. doi: [10.1016/j.neucom.2013.12.055](https://doi.org/10.1016/j.neucom.2013.12.055).
- [33] Z. Wang, J. Yu, A. Zhang, Y. Wang, and W. Zhao. Parametric geometric model and hydrodynamic shape optimization of a flying-wing structure underwater glider. *China Ocean Engineering*, 31(6):709–715, 2017. doi: [10.1007/s13344-017-0081-7](https://doi.org/10.1007/s13344-017-0081-7).
- [34] D. Gassier, J. Rebollo, and R. Dumonteil. Implementing a low-cost long-range unmanned underwater vehicle: the SeaDiver Glider. Technical Report, Calhoun Institutional Archive of the Naval Postgraduate School, Monterey, California, 2007.
- [35] D. Leandri, V. Nikishov, J.P. Frachet, T. Mathia, Y. Rudnyev, and E. Philippova. Undersea gliders for long-range applications. In O. Limarchenko, editor, *Hydrodynamics of Moving Objects*. Proceedings of the International Workshop, pages 142–153, Kiev, 2013.
- [36] T. Melin. *Parametric Airfoil Catalog. Part II. Göttingen 673 to YS930: An Aerodynamic and Geometric Comparison Between Parametrized and Point Cloud Airfoils*. Linköping University Electronic Press, 2013.
- [37] R.E. Sheldahl, and P.C. Klimas. Aerodynamic characteristics of seven symmetrical airfoil sections through 180-degree angle of attack for use in aerodynamic analysis of vertical axis wind turbines. Technical Report, Sandia National Laboratories, 1981. doi: [10.2172/6548367](https://doi.org/10.2172/6548367).
- [38] W. Shyy, Y. Lian, J. Tang, D. Viieru, and H. Liu. *Aerodynamics of Low Reynolds Number Flyers*. Cambridge University Press, 2007.
- [39] R.M. Hubbard. Hydrodynamics technology for an Advanced Expendable Mobile Target (AEMT). Technical Report no. 8013, Applied Physics Laboratory, University of Washington, 1980.
- [40] AnSys Fluent User’s Guide. Release 15.0. SAS IP, Inc., 2013.
- [41] C. Galiński, A. Dziubiński, and A. Sieradzki. Performance comparison of the optimized inverted joined wing airplane concept and classical configuration airplanes. *Archive of Mechanical Engineering*, 63(3):455–470, 2016. doi: [10.1515/meceng-2016-0026](https://doi.org/10.1515/meceng-2016-0026).
- [42] H. Schlichting. *Boundary-Layer Theory*. 7th edition, McGraw-Hill, 1979.
- [43] M. Grossrubatscher. Pilot’s Reference Guide. 10th edition. PilotsReference.com, 2008.